

**RESEARCH ARTICLE**

# High-Resolution and Motion-Robust Diffusion-Weighted Imaging with Self-Gated Self-Supervised Unrolled Reconstruction

Zhengguo Tan<sup>1</sup> | Patrick Liebig<sup>2</sup> | Annika Hofmann<sup>3</sup> | Frederik B Laun<sup>4</sup> | Florian Knoll<sup>3</sup>

<sup>1</sup>Michigan Institute for Imaging Technology and Translation (MIITT), Department of Radiology, University of Michigan, Ann Arbor, Michigan, USA

<sup>2</sup>Ultra-High Field Predevelopment Team, Siemens Healthcare GmbH, Erlangen, Bavaria, Germany

<sup>3</sup>Artificial Intelligence in Biomedical Engineering, Friedrich-Alexander-University Erlangen-Nuremberg, Erlangen, Bavaria, Germany

<sup>4</sup>Institute of Radiology, University Hospital Erlangen, Erlangen, Bavaria, Germany

**Correspondence**

Zhengguo Tan, Room 3111, Medical Science Unit I, 1301 Catherine St, Ann Arbor, MI 48109. Email: zgtan@med.umich.edu

**Funding Information**

German Research Foundation (DFG); projects 513220538, 512819079, project 500888779 in the Research Unit RU5534 for MR biosignatures at UHF. National Institutes of Health (NIH); grants R01EB024532 and P41EB017183.

**Summary**

High-resolution and motion-robust diffusion-weighted imaging (DWI) is clinically demanding. A self-supervised image reconstruction model that leverages spatial-diffusion complementary sampling and convolution is beneficial to high-quality clinical DWI.

**Purpose:** To develop an efficient self-supervised algorithm unrolling technique for high-resolution and motion-robust DWI.

**Methods:** We unroll the alternating direction method of multipliers (ADMM) to perform scan-specific self-supervised learning for deep DWI reconstruction.

**Results:** We demonstrate that (1) ADMM unrolling is generalizable across slices, (2) ADMM unrolling outperforms compressed sensing with locally-low rank (LLR) regularization in terms of image sharpness, tissue continuity and motion robustness, (3) ADMM unrolling enables clinically feasible inference time.

**Conclusion:** Our proposed ADMM unrolling enables whole brain DWI of 21 volumes at 0.7 mm isotropic resolution and 10 minutes scan, and shows higher signal-to-noise ratio (SNR), clearer tissue delineation, and improved motion robustness, which make it plausible for clinical translation.

**KEYWORDS:**

Diffusion weighted imaging, Image reconstruction, Machine learning, Self-supervised learning

**WORD COUNT:** XXX

## 1 | INTRODUCTION

High-dimensional magnetic resonance imaging (MRI) has been a flourishing field, focused on the acquisition, reconstruction and analysis of multi-dimensional

multi-contrast-weighted MRI data. Examples of high-dimensional MRI include but are not limited to magnetic resonance spectroscopic imaging (MRSI)<sup>1</sup>, diffusion-weighted imaging (DWI)<sup>2</sup>, and quantitative parameter mapping<sup>3,4</sup>. High-dimensional MRI, however, requires long acquisition times, making the data susceptible to subject motion and system imperfections, and imposing

high computational burden. DWI, in particular, poses challenges in the pursuit of high spatial, temporal, and angular resolution. DWI is typically acquired using the pulsed gradient spin echo diffusion-weighted sequence<sup>5</sup> followed by fast echo-planar imaging (EPI) readouts<sup>6</sup>. However, the use of long echo trains in EPI results in geometric distortion artifacts and reduced spatial resolution. Additionally, acquiring multiple diffusion directions to enhance angular resolution and to better probe tissue microstructure further extends the scan time.

Advances in parallel imaging<sup>7,8,9,10,11</sup> and compressed sensing<sup>12,13,14</sup> have enabled accelerated acquisition of high-dimensional data. Notably, the low-rank model<sup>15</sup> has been a powerful tool in dimension reduction. Typically, singular value decomposition (SVD) is used to learn a truncated temporal basis function from a large-scale physics-informed dictionary<sup>16,17,18</sup>. The temporal basis function is then integrated with the MRI forward model, i.e. the sensitivity encoding operator<sup>10</sup>, for joint reconstruction of the corresponding spatial basis images. In addition, low-rank regularization can be employed in the joint reconstruction<sup>19</sup>.

Beyond the low-rank technique, advanced neural networks, e.g., autoencoder<sup>20</sup>, have been explored for high-dimensional MRI reconstruction and proven to supply more accurate representations of high-dimensional data than SVD. Lam et al.<sup>21</sup> and Mani et al.<sup>22</sup> proposed to first learn a denoising autoencoder (DAE) model from a physics-informed simulated dictionary and then incorporate the learned DAE model as a regularizer in the alternating direction method of multipliers (ADMM)<sup>23</sup> unrolling reconstruction. Pioneered by Gregor and LeCun<sup>24</sup>, algorithm unrolling enables the use of learned deep *priors* as regularization and offers faster inference compared to iterative reconstruction methods that rely on hand-crafted regularization functions<sup>25</sup>. Algorithm unrolling has been applied to accelerated MRI reconstruction in various scenarios: including but not limited to supervised learning with fully sampled reference images<sup>26,27,28</sup>, and self-supervised learning with only undersampled data available for training<sup>29,30</sup>.

Deep neural networks are capable of learning not only regularization functions, but also MR-physics forward operators. Arefeen et al.<sup>31</sup> proposed to replace the conventional SVD-based linear subspace modeling<sup>16</sup> by the latent decoder model within DAE for improved  $T_2$ -weighted image reconstruction. The ability of DAE to learn DWI models is somewhat uncertain. DAE is composed of sequential fully connected layers with nonlinear activation functions, which may struggle with complex functions like those required for DWI signals. On the other hand, the diffusion tensor and kurtosis model<sup>32</sup>

consists of at least six tensor elements, so the diffusion-weighted signal dictionary based on these models usually requires tens of millions atoms. On the other hand, acquiring fully sampled DWI for training a regularization function is quite challenging. First, fully-sampled DWI requires much longer echo trains in EPI, which not only elongates the scan times but also reduces the signal-to-noise ratio (SNR). Second, the variety of diffusion acquisition modes necessitates a larger dataset compared to two-dimensional imaging scenarios<sup>33</sup>. As a result, self-supervised learning is better suited for DWI reconstruction.

In this work, we have developed a ADMM unrolling technique to perform scan-specific self-supervised learning and incorporate self-gated shot-to-shot phase variation estimation into the data-consistency term for deep diffusion-weighted imaging reconstruction. We demonstrate that the trained ADMM unrolling model from one single slice can be applied to all other slices. This significantly reduces the training time. We achieve navigator-free high-resolution DWI with 21 diffusion-encoding directions at 0.7 mm isotropic resolution, a scan time of under 10 minutes, and a reconstruction time of about 1 minute per slice.

## 2 | METHODS

### 2.1 | Multi-Band Multi-Shot DWI with Diffusion-Shift Encoding

Our previous work<sup>34</sup> demonstrated the joint  $k$ - $q$ -slice reconstruction for multi-band multi-shot navigator-based interleaved EPI (NAViEPI) DWI acquisition with diffusion-shift encoding. As show in Figure 1, the starting  $k_y$  line for a diffusion encoding is shifted with respect to its adjacent one to create complementary  $k$ - $q$ -slice sampling pattern. In the joint reconstruction, the forward model maps the multi-slice multi-diffusion-weighted images ( $\mathbf{x}$ ) to their corresponding  $k$ -space,

$$\mathcal{A}(\mathbf{x}) = \mathbf{P}\Sigma\Theta\mathbf{F}\mathbf{S}\Phi\mathbf{x} \quad (1)$$

Here, the images  $\mathbf{x}$  are point-wise multiplied with the pre-computed shot-to-shot phase variation maps ( $\Phi$ ) and coil sensitivity maps ( $\mathbf{S}$ ). The output images are then converted to  $k$ -space via two-dimensional fast Fourier transform ( $\mathbf{F}$ ), point-wise multiplied with the multi-band phases ( $\Theta$ ), summed along the slice dimension ( $\Sigma$ ), and then multiplied by the  $k$ -space undersampling mask ( $\mathbf{P}$ ).

In Equation (1), one challenge is to accurately estimate the shot-to-shot phase variation. Multiplexed sensitivity-encoding (MUSE) type reconstruction techniques<sup>35,36,37,38</sup> achieved the self-gating strategy, where

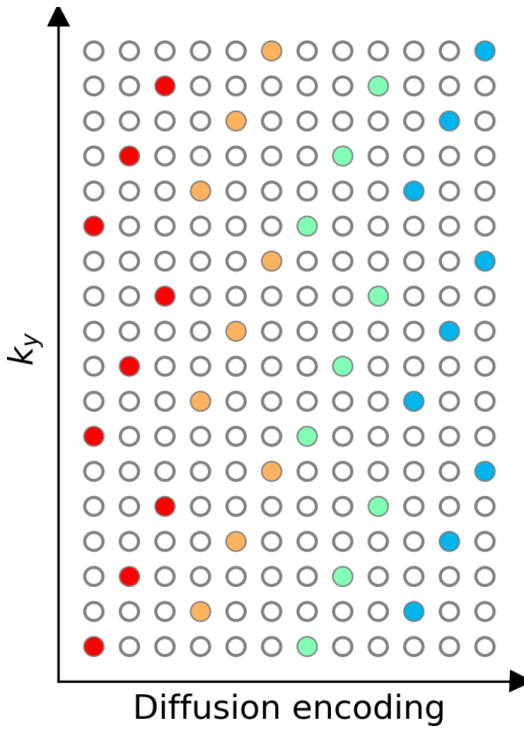


**FIGURE 1** Multi-shot DWI with diffusion shift encoding. This work employs 3-shot per diffusion encoding and each shot has an in-plane undersampling factor of 6. Therefore, every three columns have the same color. The starting  $k_y$  line is shifted between adjacent diffusion encoding to create complementary  $k$ - $q$ -space sampling.

the  $k$ -space data of each shot were used to reconstruct its corresponding shot image followed by a phase smoothing approach. Self-gated shot phase estimation does not require the acquisition of phase navigator data. However, it requires small undersampling factors per shot and fully-sampled DWI acquisition assembling all shots. Alternatively, undersampled DWI acquisition can be enabled via the acquisition of navigators for shot phase estimation<sup>34</sup>. This approach allows for mesoscale-resolution DWI at 7T, but still needs long scan time. As listed in Table 1, the total acquisition of Protocol #1 at 0.7 mm isotropic resolution takes 16 : 27 minutes with phase navigators. This scan time can be reduced to approximately 10 minutes by removing the phase navigators (Protocol #2 in Table 1).

With the operator  $\mathcal{A}$ , the joint reconstruction reads,

$$\operatorname{argmin}_{\mathbf{x}} \|\mathbf{y} - \mathcal{A}(\mathbf{x})\|_2^2 + \lambda \mathcal{R}(\mathbf{x}) \quad (2)$$

where  $\mathbf{y}$  is the measured  $k$ -space data. The first term in Equation (2) presents the data-consistency term, and the second term presents the regularization function  $\mathcal{R}(\mathbf{x})$  with the regularization strength  $\lambda$ . When using the Tikhonov regularization, i.e.  $\mathcal{R}(\mathbf{x}) = \|\mathbf{x}\|_2^2$ , Equation (2) can be solved via the conjugate gradient (CG) method.

For nonlinear regularization functions, such as the locally-low rank (LLR) regularization<sup>34</sup> or neural networks with nonlinear activation functions. ADMM was employed in this work to solve for Equation (2).

## 2.2 | Image Reconstruction via Self-Supervised ADMM Unrolling

---

### Algorithm 1 Self-Supervised ADMM Unrolling

---

```

1: Initialization:
2:   split sampling mask  $\mathbf{P}$  into 12 repetitions, each of
   which consists of three disjoint sets  $\mathbf{T}$ ,  $\mathbf{L}$ , and  $\mathbf{V}$ 
3:    $p \leftarrow 0$  and  $N_{\text{epoch}} \leftarrow 100$ 
4:    $\mathcal{D}_\omega$  set as ResNet
5:    $\rho \leftarrow 0.05$  and  $\lambda \leftarrow 0.05$ 
6:    $\text{Loss}_{\text{valid}} \leftarrow \inf$  and  $\text{trace} \leftarrow 0$ 
7: function ADMM(mask)
8:    $\mathcal{A}_{\text{mask}} \leftarrow$  set the mask in the forward operator  $\mathcal{A}$ 
9:    $\mathbf{x}^{(0)} \leftarrow \mathcal{A}_{\text{mask}}^H(\mathbf{y})$ 
10:   $\mathbf{v}^{(0)} \leftarrow \mathbf{x}^{(0)}$  and  $\mathbf{u}^{(0)} \leftarrow \mathbf{0}$ 
11:   $k \leftarrow 0$  and  $N_{\text{unroll}} \leftarrow 8$ 
12:  while  $k < N_{\text{unroll}}$  do
13:     $\mathbf{x}^{(k+1)} \leftarrow$  conjugate gradient with 6 iterations
14:     $\mathbf{v}^{(k+1)} \leftarrow (\lambda/\rho) \cdot \mathcal{D}_\omega(\mathbf{x}^{(k+1)} + \mathbf{u}^{(k)})$ 
15:     $\mathbf{u}^{(k+1)} \leftarrow \mathbf{u}^{(k)} + \mathbf{x}^{(k+1)} - \mathbf{v}^{(k+1)}$ 
16:     $k \leftarrow k + 1$ 
17:  end while
18:  return  $\mathbf{x}^{(k+1)}$ 
19: end function
20: Training:
21: while  $p < N_{\text{epoch}}$  or  $\text{trace} \leq 12$  do
22:    $\mathbf{x}_t \leftarrow \text{ADMM}(\mathbf{T})$ 
23:    $\text{Loss}_{\text{train}} \leftarrow \mathcal{L}(\mathbf{Ly}, \mathcal{A}_{\mathbf{L}}(\mathbf{x}_t))$ 
24:   update  $\omega$  via ADAM
25: Validation:
26:    $\mathbf{x}_t \leftarrow \text{ADMM}(\mathbf{T} \cup \mathbf{L})$ 
27:    $\text{Loss}_{\text{temp}} \leftarrow \mathcal{L}(\mathbf{Vy}, \mathcal{A}_{\mathbf{V}}(\mathbf{x}_t))$ 
28:   if  $\text{Loss}_{\text{temp}} \leq \text{Loss}_{\text{valid}}$  then
29:      $\text{Loss}_{\text{valid}} \leftarrow \text{Loss}_{\text{temp}}$ 
30:      $\text{trace} \leftarrow 0$ 
31:   else
32:      $\text{trace} \leftarrow \text{trace} + 1$ 
33:   end if
34: end while

```

---

Instead of the two-step alternating minimization unrolling scheme as used in MoDL<sup>28</sup>, we employed the ADMM unrolling to solve the self-supervised learning reconstruction in Equation (2). The update rule of

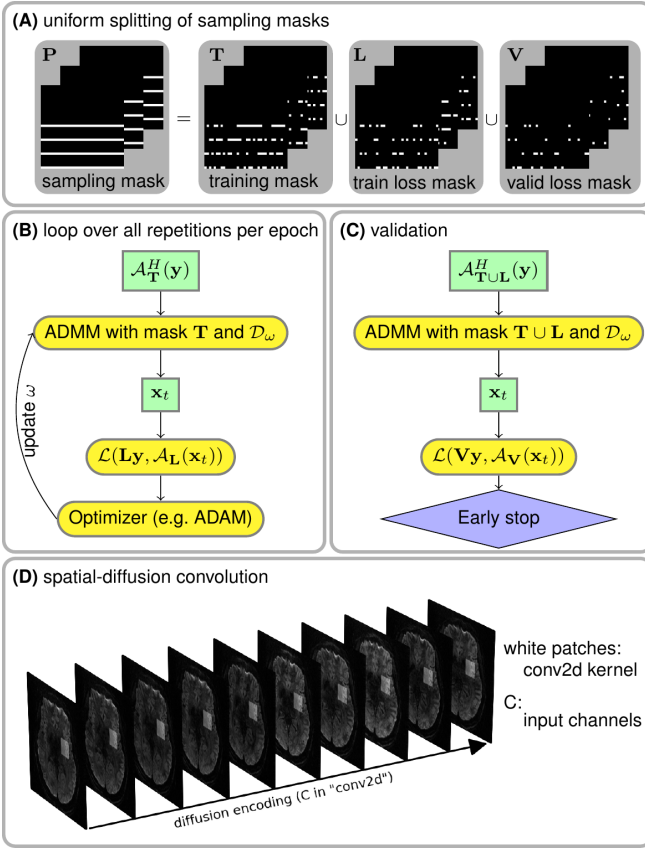


**FIGURE 2** Illustration of the key components in ADMM unrolling. **(A)** The sampling mask  $P$  in Equation (1) was uniformly split into three disjoint sets: the training mask  $\mathbf{T}$  used for the data consistency term during training, the train loss mask  $\mathbf{L}$  used for the loss function calculation during training, and the validation loss mask  $\mathbf{V}$  used for the loss function calculation during validation. **(B)** and **(C)** show the flowchart for the training and the validation of an unrolled ADMM model, respectively. Note that the ResNet parameters  $\omega$  are updated via ADAM<sup>39</sup> during training, but remain fixed during the validation step. **(D)** A stack of diffusion-weighted images is input into ResNet during ADMM unrolling.

ADMM unrolling reads

$$\begin{cases} \mathbf{x}^{(k+1)} = \underset{\mathbf{x}^{(k)}}{\operatorname{argmin}} \left\| \mathbf{y} - \mathcal{A}(\mathbf{x}^{(k)}) \right\|_2^2 + \frac{\rho}{2} \left\| \mathbf{x}^{(k)} - \mathbf{v}^{(k)} + \mathbf{u}^{(k)} \right\|_2^2 \\ \mathbf{v}^{(k+1)} = (\lambda/\rho) \cdot \mathcal{D}_\omega(\mathbf{x}^{(k+1)} + \mathbf{u}^{(k)}) \\ \mathbf{u}^{(k+1)} = \mathbf{u}^{(k)} + \mathbf{x}^{(k+1)} - \mathbf{v}^{(k+1)} \end{cases} \quad (3)$$

ADMM updates the variables  $\mathbf{x}$ ,  $\mathbf{v}$ , and  $\mathbf{u}$  in an alternating scheme. It splits the unrolled reconstruction into three steps, as shown in Equation (3) and in the pseudo code of Algorithm 1. First, the updating step for  $\mathbf{x}$  is solved by conjugate gradient. Second, the variable  $\mathbf{v}$  is then updated via the forward pass of the neural network  $\mathcal{D}_\omega$  with the input as the sum of current estimates of  $\mathbf{x}$

and  $\mathbf{u}$ . Third, the variable  $\mathbf{u}$  is updated by adding its current estimate to the difference between  $\mathbf{x}$  and  $\mathbf{v}$ .

As shown in Figure 2, to train an unrolled ADMM model, the data sampling mask  $\mathbf{P}$  is split into three disjoint sets, the training mask  $\mathbf{T}$  for the data consistency term, the training loss mask  $\mathbf{L}$  for the loss function calculation, and the validation loss mask  $\mathbf{V}$ . Each set consists of 12 repetitions constructed via random uniform sampling of the data mask  $\mathbf{P}$ . In each training epoch, every repetition is looped through in order to update the ResNet parameters  $\omega$ . Plus, the validation step is performed after every training epoch to update the minimal validation loss. If the validation loss does not reduce for 12 consecutive epochs or if 100 epochs are reached, the training is terminated.

The index  $k$  in Equation (3) denotes the unrolling iteration, and  $\mathcal{D}_\omega$  denotes the ResNet<sup>40</sup> parameterized by  $\omega$ . In this work, 2D convolution was employed to construct the ResNet layers. In PyTorch, 2D convolution requires four-dimensional tensors as input and output. For instance, a matrix with the size  $(N, C, H, W)$  is acceptable for the 'conv2d' function in PyTorch. Here,  $W$  and  $H$  denote the width and height of the convolution kernel,  $C$  denotes the number of channels, and  $N$  denotes the batch size. However, the diffusion-weighted images ( $\mathbf{x}$ ) to be reconstructed has the size  $(N_{\text{diff}}, N_Z, N_Y, N_X, 2)$ , where 2 stands for the real and imaginary part of the complex-valued diffusion-weighted images,  $N_X$  and  $N_Y$  are the width and the height of diffusion-weighted images,  $N_Z$  is the number of slices (identical to the multi-band factor), and  $N_{\text{diff}}$  is the number of diffusion encoding. To train a ResNet based on 2D convolution, the diffusion-weighted images were reshaped and permuted as  $(N_Z, 2 \cdot N_{\text{diff}}, N_Y, N_X)$ , as illustrated in Figure 2 (D). In this manner, 2D convolution kernels in combination with ReLU activation functions loop through the varying diffusion-weighted contrast to learn the key features of the high-dimensional data and to reduce noisy and aliasing artifacts in unrolled reconstruction.

## 2.3 | Model Generalizability

Volumetric whole brain DWI acquisition consists of many multi-band slices, and the training of algorithm unrolling models on all slices requires hundreds of GPU computing hours. To investigate the model generalizability and to accelerate reconstruction, we performed two training and inference strategies. First, we trained the ADMM unrolling model with only one multi-band slice data, and then tested the model on all remaining multi-band slices. We dubbed this approach as

01 "single-slice training". Second, we trained and tested  
 02 every multi-band slice individually, which was dubbed as  
 03 "slice-by-slice training". The single-slice training strategy  
 04 saves tremendous computing time, as its model is learned from one single slice and the inference time per  
 05 slice is only about one minute. By comparing these two  
 06 training strategies, we aim at demonstrating the model  
 07 generalizability and its applicability to other slices which  
 08 are "unseen" in single-slice training.

## 11 2.4 | Comparison of Regularization 12 Techniques

13 This work compared the reconstruction performance of  
 14 three different regularization techniques, Tikhonov  $\ell^2$   
 15 regularization (as used in MUSE), LLR regularization,  
 16 and ADMM unrolling with a learned regularization. Note  
 17 that MUSE is a simultaneous multi-slice (SMS) parallel  
 18 imaging method and poses no regularization along the  
 19 diffusion dimension, effectively solving each DWI  
 20 reconstruction independently. In contrast, all the other  
 21 two regularized reconstructions fall into the joint recon-  
 22 struction regime. They jointly reconstruct all diffusion-  
 23 weighted images and impose regularization terms exploring  
 24 spatial-diffusion redundancies. For example, LLR  
 25 enforces the low rankness of local spatial-diffusion matrices  
 26 from diffusion-weighted images, whereas ADMM  
 27 unrolling learns a regularization function composed by  
 28 neural networks based on spatial-diffusion convolution  
 29 kernels while enforcing data consistency during the  
 30 unrolled training process.

## 33 2.5 | In Vivo Acquisition and 34 Reconstruction

35 Table 1 lists two acquisition protocols implemented on  
 36 a clinical 7 T MR system (MAGNETOM Terra, Siemens  
 37 Healthineers, Erlangen, Germany) equipped with a 32-  
 38 channel head coil (Nova Medical, Wilmington, MA,  
 39 USA) and the XR-gradient system (maximum gradient  
 40 strength 80 mT/m and a peak slew rate 200 T/m/s).  
 41 Protocols #1 and #2 realized mesoscale high-resolution  
 42 DWI with 0.7 mm isotropic resolution. Two-fold acceler-  
 43 ation is employed in both in-plane and slice directions.  
 44 Every Diffusion encoding is acquired by three shots in  
 45 an interleaved manner and is shifted with respect to its  
 46 former one, which results in 6  $\times$  2-fold acceleration per  
 47 shot. Noteworthy, the total scan time can be reduced  
 48 to about 10 minutes (Protocol #2) when switching off  
 49 navigator acquisition.

50 **TABLE 1** NAViEPI acquisition protocols

Protocol	#1	#2
Diffusion mode	MDDW	54
Diffusion scheme	monopolar	55
Diffusion direction	20	56
$b$ -value (s/mm $^2$ )	1000	57
$b_0$	1	58
FOV (mm $^2$ )	200	59
Matrix size	286 $\times$ 286 $\times$ 176	60
Voxel (mm $^3$ )	0.7 $\times$ 0.7 $\times$ 0.7	61
Shots	3	62
Acceleration	2 $\times$ 2	63
Partial Fourier	5/8	64
Bandwidth (Hz/Pixel)	972	65
ESP (ms)	1.17	66
Navigator	Yes	No
TE (ms)	58/98.3	67
TR (ms)	15000	68
Acquisition (min)	16 : 27	69
		70
		71
		72
		73
		74
		75
		76
		77
		78
		79
		80
		81
		82
		83
		84
		85
		86
		87
		88
		89
		90
		91
		92
		93
		94
		95
		96
		97
		98
		99
		100
		101
		102
		103
		104
		105
		106

Three young healthy volunteers with written informed consent approved by the local ethics committee participated in this study. All reconstructions in this work were done on a single A100 SXM4/NVLink GPU with 80 GB memory (NVIDIA, Santa Clara, CA, USA).

## 3 | RESULTS

### 3.1 | Model Generalizability

Figure 3 demonstrates the generalizability of the proposed ADMM unrolling approach, i.e., an unrolled ADMM model trained on one single slice is applicable to all remaining "unseen" slices. Single-direction diffusion-weighted images from both the slice-by-slice training and the single-slice training strategies are displayed. The absolute difference between these two images shows no residual structural information, but mainly noise. Further, we plotted the mean and standard deviation within the selected region-of-interest (colored boxes in Figure 3 ) along all diffusion encoding. This again proves the cross-slice generalization of the proposed ADMM unrolling method. The plotted curves show quantitatively similar values between the two training strategies. With this, all following results were obtained utilizing the single-slice training strategy.

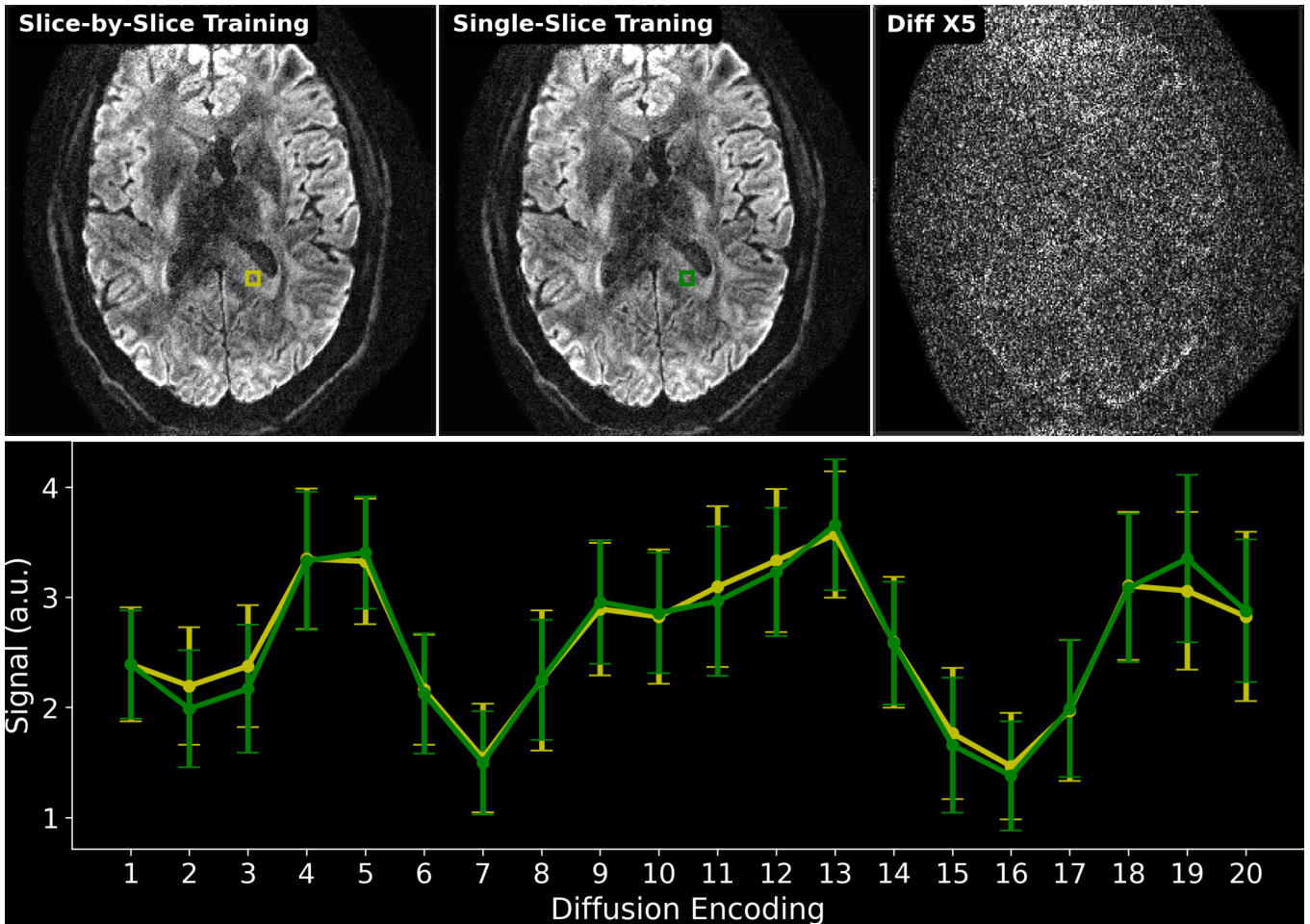


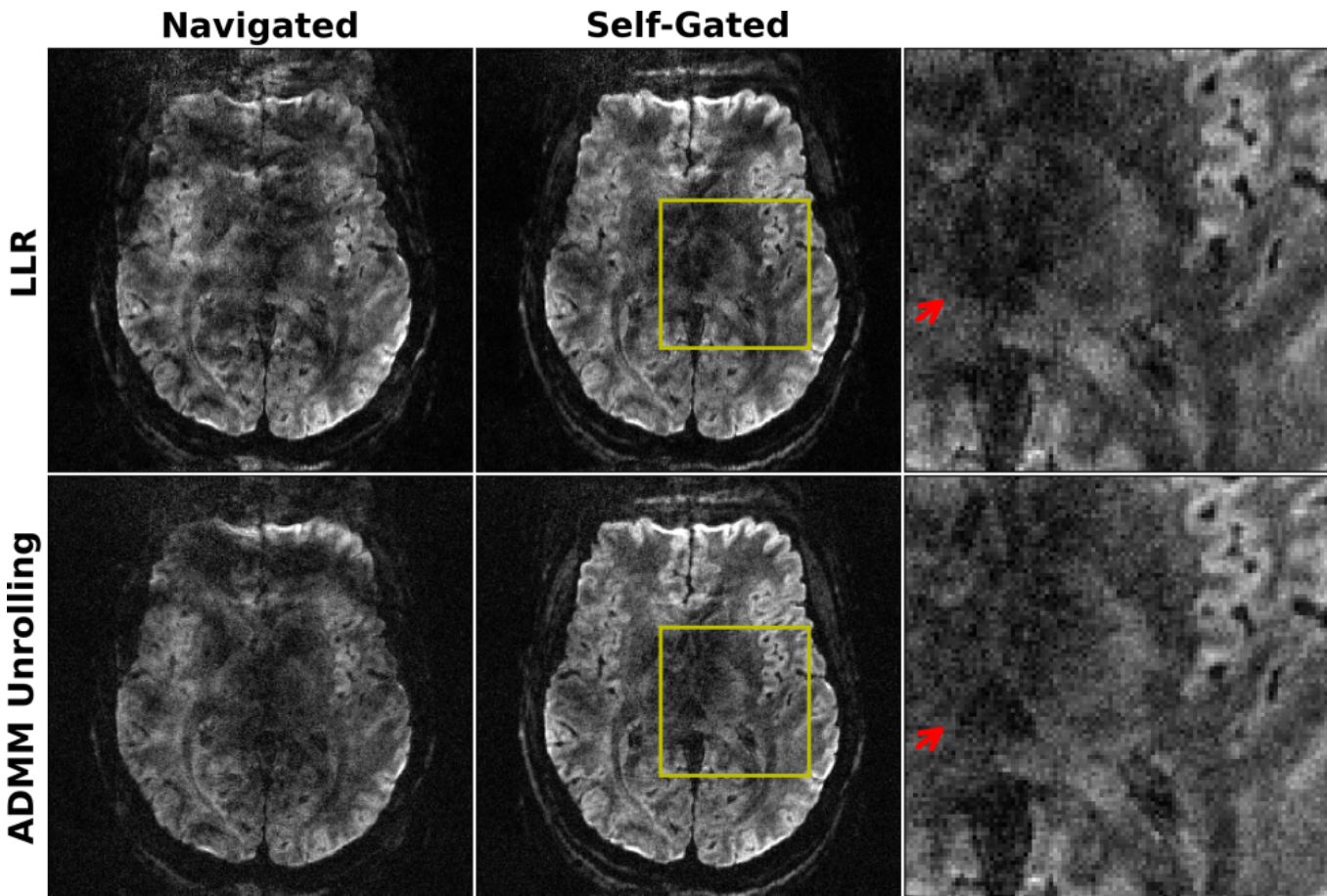
**FIGURE 3** Comparison of two training strategies: (1) slice-by-slice training, where every slice is trained and tested individually; (2) single-slice training, where the unrolled ADMM model is trained on only one slice and tested on all remaining slices. The top-right image shows the absolute difference between the reconstructed diffusion-weighted images at the 10th diffusion direction between (1) and (2). The bottom panel plots the mean and standard deviation of the signal within yellow and green rectangles in the slice-by-slice training and the single-slice training, respectively. No major qualitative or quantitative difference can be seen between the two training strategies.

### 3.2 | Retrospectively Self-Gated ADMM Unrolling

Figure 4 demonstrates the efficacy of the self-gated self-supervised ADMM unrolling reconstruction by comparing to the navigated and self-gated reconstructions on the first volunteer. Data were acquired by the NAViEPI sequence, as listed in Protocol #1 in Table 1. The single-direction diffusion-weighted images with accidental motion are displayed.

The selected diffusion encoding shows residual aliasing-like and severe motion-blurring artifacts in the navigated reconstructions, including both LLR regularization and ADMM unrolling. The main reason of these artifacts is that the acquisition of navigators increases the total scan time, resulting in higher sensitivity to accidental inter-shot motion. Admittedly, navigators are

valuable in the case of ultra high spatial resolution using many shots, e.g. 3-fold in-plane undersampling and 5-shot acquisition for the in-plane resolution of 0.5 mm<sup>34</sup>, which led to an in-plane acceleration of 15 per shot. In contrast, this experiment utilized 3 shots, yielding 6 × 2-fold acceleration per shot (refer to Protocol #1). Such an acceleration rate proves achievable in the self-gated approach. Both LLR regularized and unrolled ADMM reconstructions supply geometrically correct diffusion-weighted images without noticeable aliasing artifacts. This in turn indicates that motion corrupted the navigator data in this measurement. Further, self-gated ADMM unrolling exhibits much clearer tissue delineation in reconstructed diffusion-weighted images, as indicated by red arrows in the zoomed-in views in Figure 4, whereas self-gated LLR suffers from slightly blurry tissue boundaries and ambiguous signals.



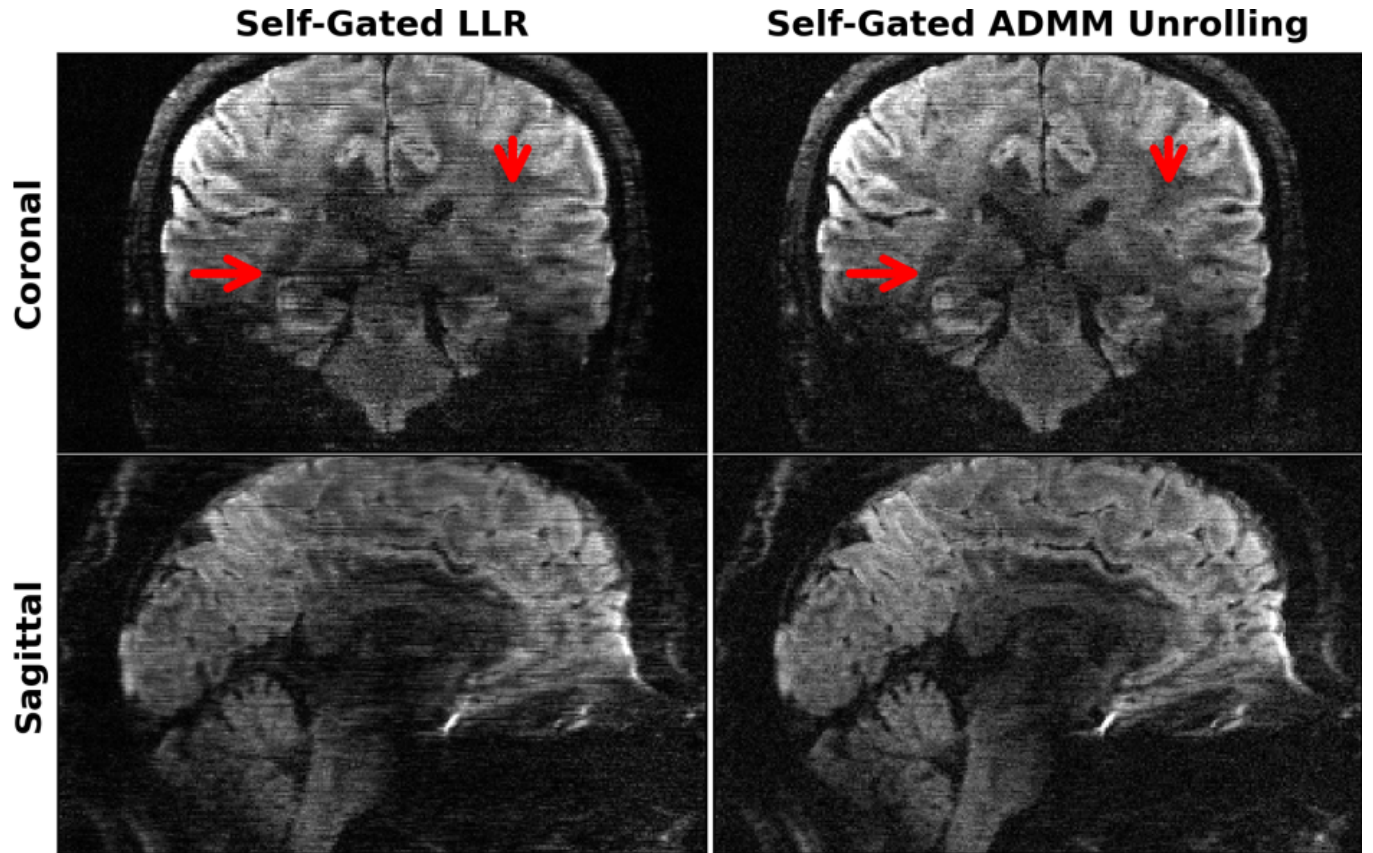
**FIGURE 4** Comparison of (top) LLR regularized and (bottom) ADMM unrolling reconstruction on 0.7 mm isotropic resolution DWI acquired by Protocol #1 with shot phase estimated from (left) navigators and (middle) imaging echoes, respectively. Zoomed views of the yellow boxes from the self-gated reconstruction are displayed in the right-most column. The use of navigators prolongs the total scan time, and thus increases the sensitivity to motion, as shown in the single-direction diffusion-weighted image reconstructed with navigated shot phase, where accidental motion occurred during navigator acquisition. The retrospectively self-gated reconstruction discards navigators, and renders sharper diffusion-weighted images. Compared to LLR, unrolled ADMM is advantageous in resolving clearer tissue boundaries in diffusion-weighted images, as indicated by red arrows.

Figure 5 shows coronal- and saggital-view diffusion-weighted images with the same diffusion encoding as in Figure 4. As mentioned in Section 2.3, the unrolled ADMM model was trained using only one slice and then inferred on all remaining slices. The model generalizes well across slices. The inference of every slice takes only about one minute, whereas the LLR reconstruction takes about 48 minutes per slice. More importantly, the self-gated LLR reconstruction exhibits residual motion-induced stripping artifacts (refer to red arrows in Figure 5)<sup>41</sup>, whereas the self-gated ADMM unrolling approach substantially removes these artifacts and supplies high-quality diffusion-weighted images without the need of navigators. Both reconstructions show  $B_1$  field inhomogeneities in the cerebellum region and residual spatial distortion in the frontal brain region. These artifacts, however, are beyond the scope of this work.

### 3.3 | Prospectively Self-Gated ADMM Unrolling

Figure 6 compares the reconstruction results using the prospectively acquired iEPI data without navigators of the second volunteer (refer to Protocol #2 in Table 1). The snapshot single diffusion-direction diffusion-weighted images as well as mean diffusion-weighted images at three orthogonal views were displayed.

The MUSE reconstruction suffers from strong noise at such mesoscale voxel size. Its corresponding mean diffusion-weighted images show improved the visibility of brain tissues, but the overall image quality is not sufficient. The LLR regularized reconstruction largely reduces noise, but still exhibits suspicious dark signal in the axial view, which appears as striping artifacts in the



**FIGURE 5** Single-direction diffusion-weighted images at 0.7 mm isotropic resolution as reconstructed by retrospectively self-gated (left) LLR and (right) ADMM unrolling in (top) the coronal and (bottom) the sagittal views, respectively. The same diffusion direction as in Figure 4 is chosen for display. ADMM unrolling reduces phase ambiguities in the shot-combined reconstruction, thereby rendering clearer tissue delineation and reducing stripping artifacts (as indicated by the red arrows).

coronal and the sagittal views (refer to the red arrows in Figure 6). On the other hand, the LLR regularized reconstruction shows amplified noise in the cerebellum region (refer to the blue arrow in the sagittal view of Figure 6), which could be caused by the  $B_1$  excitation field inhomogeneity at 7T.

The above-mentioned striping artifacts are nearly gone in the unrolled ADMM reconstruction. Moreover, the diffusion-weighted images from ADMM unrolling in the axial view show clearer diffusion contrasts and thus better tissue delineation and continuity in the coronal and the sagittal views. Further, as indicated by the blue arrows in Figure 6, the diffusion-weighted image in the sagittal view shows more homogeneous signal distribution and reduced noise surrounding the cerebellum.

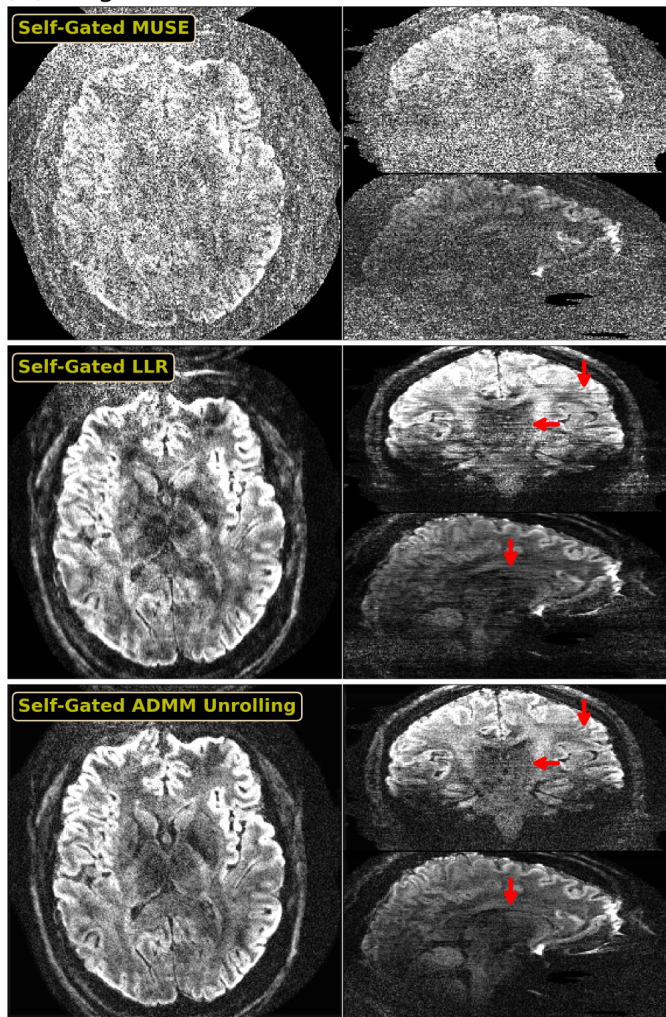
Figure 7 displays the training and validation loss as well as the learned regularization strength along epochs for the results shown in Figure 6. It can be seen that 100 epochs are sufficient for the convergence of ADMM unrolling. The model converges well along epochs, and does not show any over-fitting behavior (The validation

loss decays similarly as the training loss). In addition, the regularization strength converges to the value of about 0.027.

Figure 8 shows the reconstructed diffusion-weighted images at four different diffusion directions based on the iEPI data acquired from the third volunteer (the same subject as in Figure 3). In this experiment, the volunteer was instructed to keep still during scan. Again, the proposed self-gated ADMM unrolling reconstruction with spatial-diffusion convolution illustrates superior tissue structure delineation and diffusion contrasts to the LLR regularized reconstruction. The LLR reconstruction suffers from amplified noise in the frontal brain region. In contrast, the unrolled ADMM approach generally illustrates more homogeneous signal and noise distribution across the field-of-view. While LLR builds upon one single linear transformation (singular-value decomposition, SVD) and one nonlinear operation (soft thresholding)<sup>15</sup>, the ResNet in ADMM unrolling builds upon multiple two-dimensional convolutions and nonlinear activation functions. Therefore, deep neural networks

## 0.7 mm mesoscale DWI with 21 volumes @ 10 minutes

(A) Single-dir. DWI



(B) Mean DWI from 20 directions

enable more in-depth exploration of key features in the high-dimensional data.

## 4 | DISCUSSION

This work reported a novel self-gated self-supervised learning approach based on ADMM unrolling for multi-shot undersampled iEPI acquisition and high-resolution DWI reconstruction. The self-gated ADMM unrolling achieved whole brain DWI with 20 diffusion-encoded directions and a  $b$ -value of  $1000 \text{ s/mm}^2$  at 0.7 mm

isotropic resolution, all within a scan time of less than 10 minutes. For comparison, the compressed sensing reconstruction with locally-low rank regularization was implemented also with the generic ADMM algorithm. Thus, our work assured fair comparison among different regularization methods.

The proposed self-gated ADMM unrolling approach is well-suited for online reconstruction deployment. Firstly, it requires much shorter acquisition time than the conventional MUSE approach with fully-sampled iEPI and our previous NAViEPI method. Secondly, it does

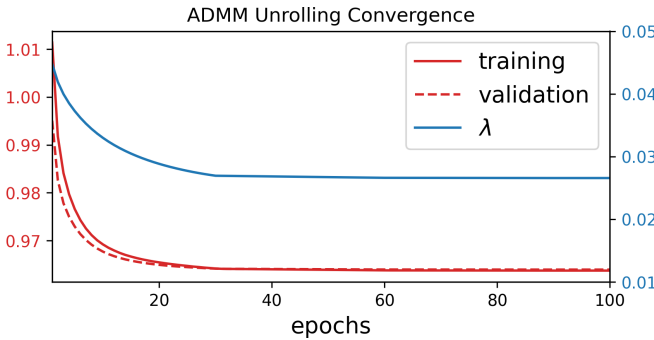


**FIGURE 7** Convergence analysis along the ADMM unrolling training and validation epochs for the results in Figure 6 . Displayed curves are (red solid) the training loss, (red dashed) the validation loss, and (blue solid) the learned regularization strength  $\lambda$ , respectively. All parameters converge sufficiently and show no over-fitting.

not require large-scale fully-sampled data for training. Instead, its training is scan specific and requires only one slice. The trained ADMM unrolling model is applicable to different slices. Third, the inference time of the trained model is much shorter compared to the LLR regularization approach.

We observed that stripping-type motion artifacts occurred more frequently in the sub-millimeter isotropic resolution DWI regime. In addition, sub-millimeter isotropic voxel resulted in higher noise in diffusion-weighted images. This makes sense, as scans with reduced slice thickness are more susceptible to shot-to-shot phase variations. To enable sub-millimeter mesoscale DWI, Setsompop et al.<sup>42</sup> proposed the gSlider technique with slice phase-dither encoding, which excites one slab multiple times with complementary slice encoding schemes. gSlider has been proven effective in alleviating motion sensitivity, because the thicker slab (in comparison to the thin single slice) reduced inter-slice motion. Meanwhile, Hadamard encoding of the slices within a slab gained SNR in the linear inverse reconstruction. However, it has been reported that gSlider has stricter requirements on  $B_0$  and  $B_1$  field homogeneities and shows residual slab boundary artifacts<sup>43</sup>. In contrast, the proposed self-gated self-supervised ADMM unrolling method requires no such advanced slab encoding, while achieves sub-millimeter resolution at a clinical feasible reconstruction time. Thus, the proposed method can be useful for the probe to high-resolution brain micro-structures in the human connectome project<sup>44</sup>. On the other hand, since unrolled algorithms are flexible to MR physics modeling (e.g., the forward operator  $\mathcal{A}$ ), the proposed ADMM unrolling can be extended to incorporate with the gSlider encoding model for enhanced SNR performance.

This work demonstrated the capability of self-gated ADMM unrolling in reconstructing 0.7 mm isotropic resolution 3-shot iPPI DWI with  $(6 \times 2)$ -fold acceleration per shot. However, we also observed that the self-gated approach failed to recover aliasing-free diffusion-weighted images in the case of higher acceleration factors (e.g. the  $0.5 \times 0.5 \times 2.0$  mm<sup>3</sup> DWI data with an acceleration of  $15 \times 2$  per shot). To address this issue, acquiring shot-to-shot phase navigators helps with the shot-combined DWI reconstruction<sup>34</sup>. Therefore, the utilization of navigator acquisition and advanced deep learning reconstruction should be application oriented. For ultra-high spatial resolution that requires many shots, navigator is needed. For the 0.7 mm resolution with 3 shots as shown in this work, the self-gated acquisition is beneficial of reducing scan time, given the superior performance of the proposed ADMM unrolling reconstruction. Alternatively, employing optimized trajectories with a more densely-sampled  $k$ -space central region could help better estimate shot phase variations<sup>35,45</sup>.

This work did not incorporate off-resonance correction in the reconstruction. As a logic extension, the multi-shot sequence can be modified to encode dynamic  $B_0$  field variation, which can then be employed in the SENSE-based forward operator and reconstruction. An established approach is known as the blip-up/down encoding<sup>46</sup>. This approach requires the acquisition of two images with opposing phase-encoding polarities (i.e., blip-up and blip-down) for the computation of  $B_0$  field maps. An alternative approach is to iteratively update  $B_0$  field based on the phase difference among acquired multiple echoes<sup>47</sup>. This approach does not require the pre-determination of  $B_0$  field, but poses higher computational demand in the inversion course of phase increments from every echo.

## 5 | CONCLUSIONS

In this work, we proposed a self-gated self-supervised learning reconstruction framework based on ADMM unrolling for high-resolution and motion-robust diffusion-weighted imaging at ultra-high field. Based on the mechanism of data splitting (cross validation), our proposed ADMM unrolling requires only one single slice for training and is generalized cross-slice. Plus, ADMM unrolling renders ultra-short inference / reconstruction time, and is thus feasible for clinical translation.

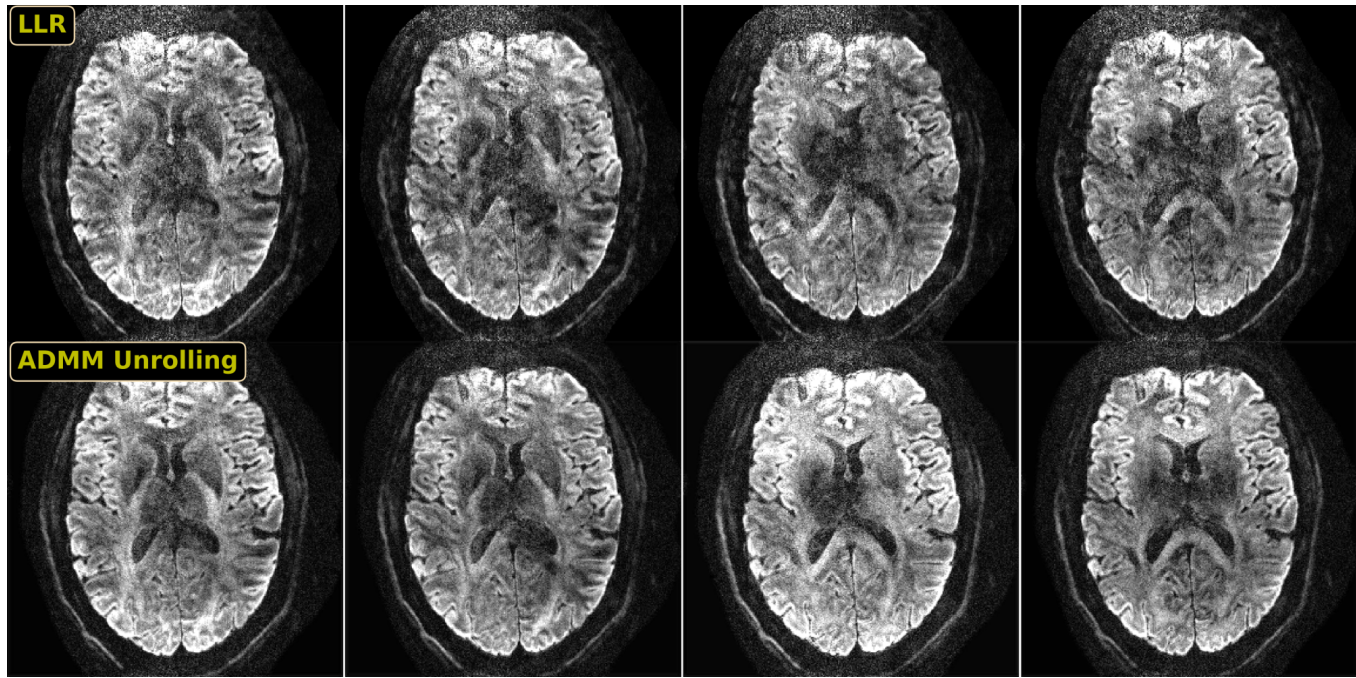


**FIGURE 8** Prospectively self-gated DWI reconstruction results at 0.7 mm isotropic resolution. Displayed images are one axial slice at four different diffusion-encoding directions. ADMM unrolling enables much cleaner delineations of diffusion contrasts than LLR regularized reconstruction.

## ACKNOWLEDGMENTS

This work was supported in part by German Research Foundation (DFG) under projects 513220538 and 512819079, project 500888779 in the Research Unit RU5534 for MR biosignatures at UHF, and by the National Institutes of Health (NIH) under grants R01EB024532 and P41EB017183. The authors are grateful to scientific support and HPC resources provided by the Erlangen National High Performance Computing Center (NHR) of Friedrich-Alexander-University Erlangen-Nuremberg (FAU) under the NHR project b143dc. NHR is funded by federal and Bavarian state authorities. NHR@FAU hardware is partially funded by DFG under project 440719683.

## OPEN RESEARCH

In the spirit of open science and reproducible research, source codes of this work are available in <https://github.com/ZhengguoTan/DeepDWI>. The presented 0.7 mm DWI raw  $k$ -space data is available in <https://doi.org/10.5281/zenodo.10781347> and <https://doi.org/10.5281/zenodo.13864504>.

## ORCID

Zhengguo Tan 0000-0002-4322-5109

Frederik B Laun 0000-0002-9269-5609

Florian Knoll 0000-0001-5357-8656

## REFERENCES

- Brown T. R., Kincaid B. M., Ugurbil K.. NMR chemical shift imaging in three dimensions. *Proc. Natl. Acad. Sci. USA*. 1982;79:3523-3526.
- Jones Derek K. *Diffusion MRI: Theory, methods, and applications*. Oxford University Press; 2010.
- Doneva Mariya, Börnert Peter, Eggers Holger, Stehning Christian, Sénégas Julien, Mertins Alfred. Compressed sensing for magnetic resonance parameter mapping. *Magn. Reson. Med.*. 2010;64:1114-1120.
- Ma Dan, Gulani Vikas, Seiberlich Nicole, et al. Magnetic resonance fingerprinting. *Nature*. 2013;495:187-192.
- Stejskal Edward O., Tanner John. Spin diffusion measurements: Spin echoes in the presence of time-dependent field gradient. *J. Chem. Phys.*. 1965;42:288-292.
- Mansfield Peter. Multi-planar image formation using NMR spin echoes. *J Phys C*. 1977;10:55-58.
- Roemer P B, Edelstein W A, Hayes C E, Souza S P, Mueller O M. The NMR phased array. *Magn. Reson. Med.*. 1990;16:192-225.
- Sodickson Daniel K, Manning Warren J. Simultaneous acquisition of spatial harmonics (SMASH): Fast imaging with radiofrequency coil arrays. *Magn. Reson. Med.*. 1997;38:591-603.
- Pruessmann Klaas P, Weiger Markus, Scheidegger Markus B, Boesiger Peter. SENSE: Sensitivity encoding

- for fast MRI. *Magn. Reson. Med.*. 1999;42:952-962.
10. Pruessmann Klaas P, Weiger Markus, Börnert Peter, Boesiger Peter. Advances in sensitivity encoding with arbitrary k-space trajectories. *Magn. Reson. Med.*. 2001;46:638-651.
  11. Griswold Mark A, Jakob Peter M, Heidemann Robin M, et al. Generalized autocalibrating partially parallel acquisitions (GRAPPA). *Magn. Reson. Med.*. 2002;47:1202-1210.
  12. Lustig Michael, Donoho David, Pauly John M. Sparse MRI: The application of compressed sensing for rapid MR imaging. *Magn. Reson. Med.*. 2007;58:1182-1195.
  13. Block Kai Tobias, Uecker Martin, Frahm Jens. Undersampled radial MRI with multiple coils. Iterative image reconstruction using a total variation constraint. *Magn. Reson. Med.*. 2007;57:1186-1098.
  14. Liang Zhi-Pei. Spatiotemporal imaging with partially separable functions. In: :988-991; 2007.
  15. Cai Jian-Feng, Candès Emmanuel J, Shen Zuowei. A singular value thresholding algorithm for matrix completion. *SIAM. J. Optim.*. 2010;20:1956-1982.
  16. Huang Chuan, Graff C G, Clarkson E W, Bilgin A, Altbach M I.  $T_2$  mapping from highly undersampled data by reconstruction of principal component coefficient maps using compressed sensing. *Magn. Reson. Med.*. 2012;67:1355-1366.
  17. Lam Fan, Liang Zhi-Pei. A subspace approach to high-resolution spectroscopic imaging. *Magn. Reson. Med.*. 2014;71:1349-1357.
  18. McGivney Debra F, Pierre Eric, Ma Dan, et al. SVD compression for magnetic resonance fingerprinting in the time domain. *IEEE Trans. Med. Imaging*. 2014;33:2311-2322.
  19. Tamir Jonathan I, Uecker Martin, Chen Weitian, et al.  $T_2$  shuffling: Sharp, multicontrast, volumetric fast spin-echo imaging. *Magn. Reson. Med.*. 2017;77:180-195.
  20. Hinton G. E., Salakhutdinov R. R.. Reducing the dimensionality of data with neural networks. *Science*. 2006;313:504-507.
  21. Lam Fan, Li Yahang, Peng Xi. Constrained magnetic resonance spectroscopic imaging by learning nonlinear low-dimensional models. *IEEE Trans. Med. Imaging*. 2019;39:545-555.
  22. Mani Merry, Magnotta Vincent A, Jacob Mathews. qModeL: A plug-and-play model-based reconstruction for highly accelerated multi-shot diffusion MRI using learned priors. *Magn. Reson. Med.*. 2021;86:835-851.
  23. Boyd Stephen, Parikh Neal, Chu Eric, Peleato Borja, Eckstein Jonathan. Distributed optimization and statistical learning via the alternating direction method of multipliers. *Foundations and Trends in Machine Learning*. 2010;3:1-122.
  24. Gregor Karol, LeCun Yann. Learning fast approximations of sparse coding. In: :399-406; 2010.
  25. Monga Vishal, Li Yuelong, Eldar Yonina C.. Algorithm Unrolling: Interpretable, Efficient Deep Learning for Signal and Image Processing. *IEEE Signal Processing Magazine*. 2021;38:18-44.
  26. Yang Yan, Sun Jian, Li Huibin, Xu Zongben. ADMM-CSNet: A Deep Learning Approach for Image Compressive Sensing. *IEEE Transactions on Pattern Analysis and Machine Intelligence*. 2018;42:521-538.
  27. Hammernik Kerstin, Klatzer Teresa, Kobler Erich, et al. Learning a variational network for reconstruction of accelerated MRI data. *Magn. Reson. Med.*. 2018;79:3055-3071.
  28. Aggarwal Hemant K, Mani Merry P, Jacob Mathews. MoDL: Model-based deep learning architecture for inverse problems. *IEEE Trans. Med. Imaging*. 2018;38:394-405.
  29. Yaman Burhaneddin, Hosseini Seyed Amir Hossein, Moeller Steen, Ellermann Jutta, Ügbübil Kâmil, Akçakaya Mehmet. Self-supervised learning of physics-guided reconstruction neural networks without fully sampled reference data. *Magn. Reson. Med.*. 2020;84:3172-3191.
  30. Yaman Burhaneddin, Hosseini Seyed Amir Hossein, Akçakaya Mehmet. Zero-shot self-supervised learning for MRI reconstruction. In: ; 2022.
  31. Areefen Yamin, Xu Junshen, Zhang Molin, et al. Latent signal models: Learning compact representations of signal evolution for improved time-resolved, multi-contrast MRI. *Magn. Reson. Med.*. 2023;90:483-501.
  32. Basser Peter J, Mattiello James, Le Bihan Denis. MR diffusion tensor spectroscopy and imaging. *Biophys. J.*. 1994;66:259-267.
  33. Knoll Florian, Zbontar Jure, Sriram Anuroop, et al. fastMRI: A Publicly Available Raw k-Space and DICOM Dataset of Knee Images for Accelerated MR Image Reconstruction Using Machine Learning. *Radiology: Artificial Intelligence*. 2020;2:e190007.
  34. Tan Zhengguo, Liebig Patrick Alexander, Heidemann Robin Martin, Laun Frederik Bernd, Knoll Florian. Accelerated diffusion-weighted magnetic resonance imaging at 7 T: Joint reconstruction for shift-encoded navigator-based interleaved echo planar imaging (JETS-NAVIEPI). *Imaging Neuroscience*. 2024;2:1-15.
  35. Liu Chunlei, Bammer Roland, Kim Dong-hyun, Moseley Michael E. Self-navigated interleaved spiral (SNAILS): Application to high-resolution diffusion tensor imaging. *Magn. Reson. Med.*. 2004;52:1388-1396.
  36. Uecker Martin, Karaus Alexander, Frahm Jens. Inverse reconstruction method for segmented multishot diffusion-weighted MRI with multiple coils. *Magn. Reson. Med.*. 2009;62:1342-1348.
  37. Chen Nan-Kuei, Guidon Arnaud, Chang Hing-Chiu, Song Allen W. A robust multi-shot scan strategy for high-resolution diffusion weighted MRI enabled by multiplexed sensitivity-encoding (MUSE). *NeuroImage*. 2013;72:41-47.
  38. Merrem Andreas, Hofer Sabine, Hosseini Ali Seif Amir, et al. Diffusion-weighted MRI of the prostate without susceptibility artifacts: Undersampled multi-shot turbo-STEAM with rotated radial trajectories. *NMR Biomed.*. 2019;32:e4074.
  39. Kingma Diederik P, Ba Jimmy. ADAM: A Method for Stochastic Optimization. In: ; 2015.

- 01 40. He Kaiming, Zhang Xiangyu, Ren Shaoqing, Sun Jian. □ 54  
02 Deep residual learning for image recognition. In: :770-778; 55  
03 2016. 56  
04 41. Chang Wei-Tang, Huynh Khoi Minh, Yap Pew- 57  
05 Thian, Lin Weili. Navigator-Free Submillimeter Diffusion 58  
06 MRI using Multishot-encoded Simultaneous Multi-slice 59  
07 (MUSIUM) Imaging. In: :1322; 2021. 60  
08 42. Setsopop Kawin, Fan Qiuyun, Stockmann Jason, et al. 61  
09 High-resolution *in vivo* diffusion imaging of the human 62  
10 brain with generalized slice dithered enhanced resolution: 63  
11 Simultaneous multislice (gSlider-SMS). *Magn. Reson. 64  
Med.*. 2018;79:141-151. 65  
12 43. Dai Erpeng, Liu Simin, Guo Hua. High-resolution whole- 66  
13 brain diffusion MRI at 3T using simultaneous multi-slab 67  
14 (SMSlab) acquisition. *NeuroImage*. 2021;237:118099. 68  
15 44. Huang Susie Y., Witzel Thomas, Keil Boris, et al. 69  
16 Connectome 2.0: Developing the next-generation ultra- 70  
17 high gradient strength human MRI scanner for bridging 71  
18 studies of the micro-, meso- and macro-connectome. 72  
19 *NeuroImage*. 2021;243:118530. 73  
20 45. Dai Erpeng, Lee Philip K, Dong Zijing, Fu Fanrui, 74  
21 Setsopop Kawin, McNab Jennifer A. Distortion-free 75  
22 diffusion imaging using self-navigated Cartesian echo- 76  
23 planar time resolved acquisition and joint magnitude 77  
24 and phase constrained reconstruction. *IEEE Trans Med 78  
Imaging*. 2022;41:63-74. 79  
25 46. Zahneisen Benjamin, Aksoy Murat, Maclareen Julian, 80  
26 Wuerslin Christian, Bammer Roland. Extended hybrid- 81  
27 space SENSE for EPI: Off-resonance and eddy current 82  
28 corrected joint interleaved blip-up/down reconstruction. 83  
29 *NeuroImage*. 2017;153:97-108. 84  
30 47. Tan Zhengguo, Unterberg-Buchwald Christina, Blumen- 85  
31 thal Moritz, et al. Free-breathing liver fat,  $R_2^*$  and  $B_0$  86  
32 field mapping using multi-echo radial FLASH and reg- 87  
33 ularized model-based reconstruction. *IEEE Transactions 88  
on Medical Imaging*. 2023;42:1374-1387. 89  
34 86  
35 87  
36 88  
37 90  
38 91  
39 92  
40 93  
41 94  
42 95  
43 96  
44 97  
45 98  
46 99  
47 100  
48 101  
49 102  
50 103  
51 104  
52 105  
53 106